Proceedings of the 12th International Conference on
Computational Fluid Dynamics in the Oil & Gas,
Metallurgical and Process Industries

Progress in Applied CFD – CFD2017

SINTEF

SINTEF Proceedings

Editors:
Jan Erik Olsen and Stein Tore Johansen

Progress in Applied CFD – CFD2017

Proceedings of the 12th International Conference on Computational Fluid Dynamics in the Oil & Gas, Metallurgical and Process Industries

SINTEF Academic Press

SINTEF Proceedings
SINTEF Proceedings is a serial publication for peer-reviewed conference proceedings
on a variety of scientific topics.
The processes of peer-reviewing of papers published in SINTEF Proceedings are
administered by the conference organizers and proceedings editors. Detailed
procedures will vary according to custom and practice in each scientific community.

PREFACE

This book contains all manuscripts approved by the reviewers and the organizing committee of the 12th International Conference on Computational Fluid Dynamics in the Oil & Gas, Metallurgical and Process Industries. The conference was hosted by SINTEF in Trondheim in May/June 2017 and is also known as CFD2017 for short. The conference series was initiated by CSIRO and Phil Schwarz in 1997. So far the conference has been alternating between CSIRO in Melbourne and SINTEF in Trondheim. The conferences focuses on the application of CFD in the oil and gas industries, metal production, mineral processing, power generation, chemicals and other process industries. In addition pragmatic modelling concepts and bio-mechanical applications have become an important part of the conference. The papers in this book demonstrate the current progress in applied CFD.

The conference papers undergo a review process involving two experts. Only papers accepted by the reviewers are included in the proceedings. 108 contributions were presented at the conference together with six keynote presentations. A majority of these contributions are presented by their manuscript in this collection (a few were granted to present without an accompanying manuscript).

The organizing committee would like to thank everyone who has helped with review of manuscripts, all those who helped to promote the conference and all authors who have submitted scientific contributions. We are also grateful for the support from the conference sponsors: ANSYS, SFI Metal Production and NanoSim.

Stein Tore Johansen & Jan Erik Olsen

Organizing committee:

Conference chairman: Prof. Stein Tore Johansen
Conference coordinator: Dr. Jan Erik Olsen
Dr. Bernhard Müller
Dr.Sigrid Karstad Dahl
Dr.Shahriar Amini
Dr.Ernst Meese
Dr.Josip Zoric
Dr.Jannike Solsvik
Dr.Peter Witt

Scientific committee:

Stein Tore Johansen, SINTEF/NTNU
Bernhard Müller, NTNU
Phil Schwarz, CSIRO
Akio Tomiyama, Kobe University
Hans Kuipers, Eindhoven University of Technology
Jinghai Li, Chinese Academy of Science
Markus Braun, Ansys
Simon Lo, CD-adapco
Patrick Segers, Universiteit Gent
Jiyuan Tu, RMIT
Jos Derksen, University of Aberdeen
Dmitry Eskin, Schlumberger-Doll Research
Pär Jönsson, KTH
Stefan Pirker, Johannes Kepler University
Josip Zoric, SINTEF

CONTENTS

12th International Conference on CFD in Oil & Gas, Metallurgical and Process Industries
SINTEF, Trondheim, NORWAY
May 30th - June 1st, 2017

079

A NUMERICAL APPROACH TO MODEL AGGREGATE RESTRUCTURING IN SHEAR FLOW USING DEM IN LATTICE-BOLTZMANN SIMULATIONS

Akash SAXENA[1][*], **Jean-Sébastien KROLL-RABOTIN**[2][†], **R. Sean SANDERS**[1][‡]

[1]Department of Chemical Engineering, University of Alberta, CANADA

[2]Institut Jean-Lamour, UMR 9871, CNRS, Université de Lorraine-CNRS, Nancy, FRANCE

Laboratory of Excellence for Design of Alloy Metals for Low-mass Structures, FRANCE

[*] E-mail: asaxena@ualberta.ca
[†] E-mail: jean-sebastien.kroll-rabotin@univ-lorraine.fr
[‡] E-mail: ssanders@ualberta.ca

ABSTRACT

Aggregate shape and structure significantly impact rheological properties of fluids in many fields such as extractive metallurgy, oil field drilling and mineral processing. The morphology of the aggregates determines the porosity of solid structures and their dimensions, which in turn affects the solid-liquid and solid-solid interactions in the mixture, and hence the rheology of the system. Aggregates can undergo morphological changes induced by shear flow. The response of aggregate mixtures in terms of rheology as a function of their shear history has thus been studied in many fields (Coufort *et al.*, 2005) with experimental approaches. Numerical investigations of aggregation dynamics and aggregate restructuration have also been conducted in low Reynolds conditions (Frungieri and Vanni, 2016), or using free draining approximation, in which the fluid particle interactions are exclusively through Stokesian drag (Eggersdorfer *et al.*, 2010). In this study, a fully coupled Eulerian-Lagrangian approach is developed to evaluate the restructuring of aggregates in shear flows for low Reynolds numbers. In particular, a Discrete Element Method (DEM) is used for particle tracking, coupled with Lattice Boltzmann Method (LBM) for solving the liquid flow. An Immersed Boundary Method (IBM) is incorporated so that primary particle shapes and hydrodynamic interactions between particles are fully resolved (Niu *et al.*, 2006). Selected particle-particle interaction models have been implemented in the DEM to represent the mechanical behaviour of aggregates. General attractive and repulsive force models, and the bending moment as described by Pantina and Furst (2005) have been included.

Artificial aggregates were created and characterized using fractal dimension and radius of gyration. The evolution of these shape indicators over time has been studied while aggregates are subjected to a shear flow. Preliminary results obtained with fully coupled liquid-solid simulations were also compared with results based on the free draining approximation. In fully coupled simulations, significant perturbations in the flow field were observed due to the presence of particles, which leads to a significant difference in aggregate's restructuring. Different solid interaction contributions and their underlying impact on aggregate restructuring have been compared, at a given shear rate. While increasing shear or maximum cohesion forces lead to denser aggregates, effect of tangential forces on the aggregate's morphology appears to be more complex. Also, tangential forces were found to have a tendency to favor aggregate breakage.

Keywords: Aggregates, shear flow, restructuring, CFD-DEM, free draining, lattice-Boltzmann method, immersed boundary method. .

NOMENCLATURE

Greek Symbols

α	Acceleration force coefficient,	$[kg]$.
β	Velocity force coefficient,	$[kg \cdot s]$.
γ	Force contribution,	$[N]$.
$\dot{\gamma}$	Shear rate,	$[s^{-1}]$.
ρ	Mass density,	$[kg \cdot m^{-3}]$.
μ	Dynamic viscosity,	$[Pa \cdot s]$.
ξ	Spring elongation,	$[m]$.
ω	angular velocity,	$[rad \cdot s^{-1}]$.
Ω	LBM collision operator,	$[\ ]$.
δ	Regularized Dirac function,	$[\ ]$.
Δ	Step,	$[\ ]$.

Latin Symbols

A_H	Hamaker constant,	$[J]$.
$\mathcal{A}$	Surface area,	$[m^2]$.
D_f	Fractal dimension,	$[\ ]$.
f	LBM quantities,	$[\ ]$.
f	Volume force,	$[N \cdot m^{-3}]$.
F	Force,	$[N]$.
$\mathcal{I}$	Tensor of inertia,	$[kg \cdot m]$.
m	Mass,	$[kg]$.
N	Number of particles,	$[\ ]$.
N_{Born}	Born constant,	$[\ ]$.
P	Projection matrix,	$[\ ]$.
q	LBM solution vector,	$[\ ]$.
R_g	Radius of gyration,	$[m]$.
R_p	Particle radius,	$[m]$.
S	Structure factor,	$[\ ]$.
T	Torque,	$[N \cdot m]$.
t	Time,	$[s]$.
v	Velocity,	$[m \cdot s^{-1}]$.
V	Force potential,	$[J]$.

Sub/superscripts

f	Fluid.
i	Index i.
j	Index j.
M	Marker point.
n	Normal component.
t	Tangential component.
p	Particle.

A. Saxena, J. Kroll-Rabotin, R. Sanders

INTRODUCTION

The efficiency of most industrial processes involving fluid-solid systems strongly depends on aggregate behaviours, either directly or through their impact on rheological parameters of the fluid-solid mixture. In mineral processing (Laskowski and Ralston, 2015) or liquid metal treatments (Zhang and Thomas, 2003), shear induced aggregation is often used to form bigger aggregates which are easier to recover. In extractive metallurgy as well as in the oil sand industry, aggregation of colloidal clay particles in the tailings is necessary to separate them out (Plumpton, 2013). Whatever the material they are made of, floc and aggregate properties are conditioned by the flow conditions (Vaezi G. *et al.*, 2011; Khashayar Rastegari *et al.*, 2004; Coufort *et al.*, 2005; Daoud *et al.*, 2011).

Aggregates are formed by primary particles that come sufficiently close to each other, so that they undergo cohesive forces. When they are transported in a fluid phase, they experience hydrodynamic forces that compete with the cohesive forces holding them together. Consequently, in such conditions, their morphology evolves, which impacts both the distributions of the hydrodynamic stresses and the contact/cohesive forces within the aggregate.

Early attempts to predict the aggregation kinetics are a century old, when Smoluchowski (1917) first gave the equation to predict the net rate of aggregation of particles based on collision frequency. However, his work did not explain the underlying mechanics. Earlier, due to the complexity of the physics, the aggregates were assumed to be of simple shapes such as spheres, and stresses across the sphere were calculated in shear flow to predict its rupture (Bagster and Tomi, 1974). Later, porosity of aggregates was taken into account by Adler and Mills (1979). However, it was concluded by Sonntag and Russel (1987) that this approach was not supported by experimental data as it did not take into account the complex shapes of aggregates.

With the advancements in computational resources, attempts were made to model evolution of aggregates composed of discrete particles. Using the Discrete Element Method (DEM) (Cundall and Strack, 1979), it became possible to model the forces between every primary particle. For hydrodynamic forces, free-draining approximation has been extensively used (Chen and Doi, 1989; Potanin, 1993; Becker *et al.*, 2009; Eggersdorfer *et al.*, 2010). It assumes that each particle experiences Stokesian drag as if no other particle were present in its vicinity. Brady and Bossis (1988) developed Stokesian Dynamics (SD) which accurately accounts for the impacts of hydrodynamic interactions on aggregates (Harshe *et al.*, 2011; Vanni and Gastaldi, 2011; Seto *et al.*, 2012; Harshe and Lattuada, 2012; Conchuir *et al.*, 2014; Ren *et al.*, 2015). However, SD is only valid for spheres and is accurate only for low Reynolds conditions. Schlauch *et al.* (2013) have developed a Finite Element Method (FEM) in which Stokes equation is discretized and solved over the surface. Again, this approach is limited to low Reynolds conditions, but allows complex shape primary particles. Immersed Boundary Method (IBM) (Peskin, 1972) is now being widely used for full coupling between complex shape objects and full Navier-Stokes flow solver. Different variants of IBM have proven able to handle even high Reynolds conditions (Yang and Stern, 2013; Taira and Colonius, 2007; Lācis *et al.*, 2016). Schlauch *et al.* (2013) have done a comparative study of these coupling methods (namely, FEM, SD and LBM), however, their particles were fixed in a fluid flow. Till

now, fully coupled liquid-solid simulations are still very rare due to their high computation cost, thus there remains a lack of understanding about the impact of hydrodynamic interactions on the aggregate structures.

Lattice Boltzmann methods (LBM) have proved efficient to solve the flow field around complex shapes. Binder *et al.* (2006) used LBM to compare results with accelerated SD and Schlauch *et al.* (2013) used LBM to resolve the flow around their fixed aggregates.

In various studies, different force models have been used depending on the physical system. Commonly used models include spring-dashpot model (Kadau *et al.*, 2002; Iwashita and Oda, 1998; Seto *et al.*, 2012). Other studies have used DLVO model to describe the normal forces in colloidal systems (Becker and Briesen, 2008; Becker *et al.*, 2009; Ren *et al.*, 2015; Conchuir *et al.*, 2014; Harshe *et al.*, 2011). Even magnetic models have been used is specific studies (Dominik and Nübold, 2002). Normal forces have thus been extensively studied, however, in many systems such as colloidal suspensions, tangential forces have also been observed (Pantina and Furst, 2005) and modelled (Becker and Briesen, 2008). Still, no study has been done so far to quantify the relative effect of the involved forces in restructuring of an aggregate.

From all these works that have been conducted so far, it appears that in many systems, cohesive forces between primary particles have both tangential and normal components. The way the hydrodynamic forces are balanced by the contact forces is what drives the restructuring of aggregates. It is thus expected that the relative weight of the two contributions of the cohesive force may significantly impact the morphological changes of the aggregates. Using fractal dimension to characterize aggregate morphology, we have compared the relative effect of selected forces in a shear flow. The forces that we have considered are maximum attractive force, drag force and maximum bending moment.

Due to the major role of the drag force in the problem, preliminary studies using IBM in Lattice-Boltzmann simulations have also been conducted and compared to the free-draining approximation.

SIMULATION SETUP AND NUMERICAL METHODS

Generation and characterization of initial aggregates

Aggregate size and density are the most natural quantities to characterize aggregates (Gregory, 1997). Several studies have worked on relating these two properties through the concept of fractal dimension (Gregory, 1997; Woodfield and Bickert, 2001; LI and Ganczarczyk, 1989; Bushell *et al.*, 2002). It is defined on the basis that the mass of an aggregate scales as a power of its size, this power being the fractal dimension. This allows to characterize morphology using a unique quantity. To ensure that fractal dimension is a valid way to characterize aggregate morphological evolutions, simulations have been run for 10 different aggregates with the same fractal dimension (D_f) and the same number of particles (N), namely $D_f = 2.30 \pm 0.01$, radius of gyration (R_g) = $22.76 \pm .01 \mu m$ and $N = 50$, as represented in figure 1. To estimate the fractal dimension, is has been derived from the number of particles and the radius of gyration, which are straightforward to calculate.

$$N = S \left(\frac{R_g}{R_p} \right)^{D_f} \tag{1}$$

In equation (1), S is the static structure factor, for which there
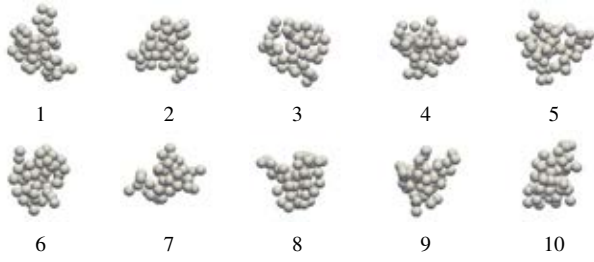
Figure 1: The 10 artificially created initial aggregates that have been used in the simulations ($N = 50$, $D_f = 2.30 \pm 0.01$), $R_g = 22.76 \pm .01 \mu m$

exists an empirical expression as a function of the fractal dimension (Gmachowski, 2002).

$$S = \left(\sqrt{1.56 - \left(1.728 - \frac{D_f}{2}\right)^2} - 0.228 \right)^{D_f} \left(\frac{2 + D_f}{D_p} \right)^{\frac{D_f}{2}} \quad (2)$$

Some studies (Harshe *et al.*, 2011) also include radius of gyration (R_g) to characterize an aggregate. However, since equation (1) includes R_g, there is no need to track it along with D_f.

The initial structures of the simulated aggregates (see figure 1) were produced algorithmically. An initial sphere is placed, then all the other spheres are added one after the other to the aggregate. Each new sphere is placed at random position relative to another existing sphere. Sixteen (16) random positions are tested for every new sphere, and the chosen position is the one that yields the fractal dimension that is closest to the target fractal dimension. This process is repeated until the aggregate contains the desired number of primary spheres.

Discrete Element Method

To study the restructuring of an aggregate, each particle has to be tracked independently. In the Discrete Element Method (DEM) (Cundall and Strack, 1979), all forces acting on every individual particle are calculated, and the equations of motion for all particles are solved.

Forces are evaluated at each time step by iterating over every individual particle and all particle pairs that are closer than a given maximum interaction distance. Then particle velocities and positions are updated. After that, the next time step starts again by calculating the forces applied to each particle, as well as computing interphase coupling forces when the liquid flow is resolved, and so on. The forces applied to each individual particles (driving forces) and to particle pairs (interaction forces) are described in the next section. Particle velocities are calculated by solving Newton's equations of motion for every particle.

$$m \frac{d\vec{v}_i}{dt} = \sum \vec{F}_i \quad (3)$$

$$\mathcal{J} \frac{d\vec{\omega}_i}{dt} = \sum \vec{T}_i \quad (4)$$

To solve these equations, we use a semi-explicit approach where all forces that depend on particle acceleration and velocity are accounted for as linear functions, represented by coefficients α and β in equation (5).

$$m_p \frac{d\vec{v}}{dt} = \alpha \frac{d\vec{v}}{dt} + \beta \vec{v} + \vec{\gamma} \quad (5)$$

The term $\vec{\gamma}$ contains the forces that do not depend on particle motion. The velocity calculation at each time step comes directly from equation (5) following a semi-implicit approach, which yields a simple linear equation.

$$m_p \frac{\vec{v}(t + \Delta t) - \vec{v}(t)}{\Delta t} =$$

$$\alpha \frac{\vec{v}(t + \Delta t) - \vec{v}(t)}{\Delta t} + \beta \vec{v}(t + \Delta t) + \vec{\gamma} \quad (6)$$

Equation (6) is solved for $\vec{v}(t + \Delta t)$.

$$\vec{v}(t + \Delta t) = \frac{\left(\frac{m_p - \alpha}{\Delta t}\right) \vec{v}(t) + \vec{\gamma}}{\frac{m_p - \alpha}{\Delta t} - \beta} \quad (7)$$

The equation for the angular moment is expressed in the same way, and it is solved similarly.

In this specific study, $\alpha = 0$ and particle inertia is negligible, so equation (7) practically boils down to $\vec{v} = -\vec{\gamma}/\beta$. However, inertia has been kept in the solver since it helps stabilize the particle motion when interaction forces see very steep variations, and it is physically there anyway. Finally, particle position is updated with the new velocity.

$$\vec{x}(t + \Delta t) = \vec{x}(t) + \Delta t \, \vec{v}(t + \Delta t) + \frac{\Delta t}{2} (\vec{v}(t + \Delta t) - \vec{v}(t)) \quad (8)$$

This integration scheme, while not being of high order accuracy, helps stabilizing the interactions between primary particles since it dissipates energy from the otherwise purely elastic interactions, but it preserves the maximum values of the different forces. Due to the low inertia of the particles, the acceleration term is negligible, except for the few time steps when new bonds are created between primary particles.

The DEM is only a tracking method for the primary particles that the aggregate is made of. All the interesting physics must be captured by the force models that are included. The forces here are of two nature, driving forces and pair particle interactions.

Forces involved

In a solid-liquid system, the dynamics of every primary particle is governed by primarily two types of interactions: interparticle forces and hydrodynamic forces.

DLVO theory has been used to represent particle interactions, which includes Van der Waals forces as cohesive forces. Normal forces then derive from a potential (V). Since the considered primary particles are spherical, a simplified form for the potential has been used (Hamaker, 1937).

$$V_{\text{VDW}}(s) = -\frac{-A_H}{12(s - 2)} \quad (9)$$

Here, A_H is the Hamaker constant, and s is the non-dimensional distance between two particles. Attractive Van der Waals forces must be balanced by a steeper very short range force that prevents particle from overlapping. Born repulsion (Feke *et al.*, 1984) plays this role.

$$V_{\text{Born}}(s) = \frac{A_H N_{\text{Born}}}{s} \left[\frac{s^2 - 14s + 54}{(s - 2)^7} \right.$$

$$\left. + \frac{60 - 2s^2}{s^7} + \frac{s^2 + 14s + 54}{(s + 2)^7} \right] \quad (10)$$

Here, N_{born} is the Born constant. When combined, these two attractive and repulsive contributions form an energy barrier that must be overcome for particles to separate. This energy barrier corresponds to a maximum attractive force.

Moreover, a tangential force has been included. This tangential force is responsible for providing a bending moment to the aggregates similar to that seen in an elastic rod (Becker and Briesen, 2008). In this model, when two particles come close and stick to each other due to cohesive forces, they interact in an elastic manner modelled by springs (k_t) whose elongation (ξ) corresponds to the relative tangential displacement of the interacting particles.

$$\frac{d\vec{\xi}_{ij}}{dt} = (1 - \vec{n}_{ij} \otimes \vec{n}_{ij})(\vec{v}_j - \vec{v}_i) - 2R_p(\vec{\omega}_j \times \vec{n}_{ij}) \quad (11)$$

where i and j are particle indices, $\vec{v}$ is their velocity, $\vec{\omega}$ is their angular velocity and n_{ij} is the unit vector pointing from the center of particle i to the center of particle j. Force and moment depend on spring elongation (ξ).

$$\vec{F}_j = k_t(\vec{\xi}_{ij} - \vec{\xi}_{ji}) \quad (12)$$

$$\vec{T}_j = 2R_p k_t \vec{n}_{ji} \times \vec{\xi}_{ji} \quad (13)$$

The maximum bending moment that particles can exert on each other is fixed through a critical elongation (d_{max}) after which springs can no longer elongate. Thus, the maximum tangential force between a pair of particles is $k_t \cdot d_{max}$.

All the values for the constants (A_H, N_{Born}, k_t and d_{max}) were chosen so that the forces cover a range that is expected for 2 μm clay particles in water. The overall set of conditions that have been tested is summarized in tables 1 and 2. (d_{max}) has been chosen as 2% of particle's diameter.

The driving forces for aggregate restructuring are hydrodynamic forces. In this study, two approaches haves been considered: Free Draining Approximation and Immersed Boundary Method.

Free Draining Approximation

In the free draining approximation, it is assumed that the hydrodynamic forces acting on a particle are not affected by the presence of other particles. They do not account for the perturbation of particles on the fluid flow. Thus, it is only a one-way coupling. It tends to overestimate the forces as it does not compensate the surface area of primary particles shielded by other particles. It is calculated using Stokes' law, since the particle Reynolds number remains small in the considered cases. A pure shear flow is imposed for the liquid phase.

$$\vec{F}_{f/p} = 6\pi\mu R_p(\vec{v}_p - \dot{\gamma}z\vec{e}_x) \quad (14)$$

$$\vec{T}_{f/p} = 8\pi\mu R_p^3(\vec{\omega}_p - \frac{1}{2}\dot{\gamma}\vec{e}_y) \quad (15)$$

where μ is the dynamic viscosity of the fluid, index p is for particle properties and $\dot{\gamma}$ is the shear rate in liquid flow.

To resolve the hydrodynamic interactions between particle, such as shielding, two-way coupling is required and a flow solver is needed. A lattice Boltzmann method has been used for that.

Lattice Boltzmann Method

Aggregate restructuring is driven by particle contacts. Interaction forces have very steep variations according to interparticle distance and collision are instantaneous events, thus

the time and the length scales induced by the particle interactions are much shorter than the ones of the liquid flow. Thus, an explicit method is well suited to solve for the fluid flow, since flow evolutions will be slow compared to other physical mechanisms that put stronger constrains on the time steps.

Lattice Boltzmann methods have become the most common explicit flow solvers. Moreover, the inherent difficulty to use complex meshes in such methods has also led to the development of several ways to represent solid boundaries inside the fluid phase, which is also a significant asset for the study of aggregate restructuring, since changes in the contacts between particle make it particularly difficult to represent particles using mesh boundaries.

For these reasons, a lattice Boltzmann method has been used for simulations in which the liquid flow was resolved. Lattice Boltzmann methods are based on the resolution of the Boltzmann equation (16) in which the flow field variables are only solved as moments of the probabilities (f) associated to a given mass at a given position in space, moving at a given velocity.

$$\frac{\partial f}{\partial t} + \vec{c} \cdot \vec{\nabla}_x f = \Omega(f) - \vec{f} \cdot \vec{\nabla}_c f \quad (16)$$

$$\rho = \int_{\mathbb{R}^3} f(\vec{c})\,d\vec{c} \qquad \rho\vec{u} = \int_{\mathbb{R}^3} \vec{c}f(\vec{c})\,d\vec{c}$$

Once discretized over a lattice, that is a finite set of positions in space and a finite set of velocities ($\vec{c}_i$) at which mass probabilities can travel from one node to its neighbours during a time step, the Boltzmann equation can be solved explicitly using a time-splitting approach, where the dynamics are solved in two steps: collision and streaming. Hereafter, external volume forces ($\vec{f}$) are accounted for during the collision step, that is, included into the so-called collision operator (Ω).

$$\overbrace{f_i(\vec{x} + \vec{c}_i\Delta t, t + \Delta t)}^{\text{streaming}} = \overbrace{f_i(\vec{x}, t) + \Omega_i\left(f(\vec{x}, t), \vec{f}(\vec{x}, t)\right)\Delta t}^{\text{collision}} \quad (17)$$

Bhatnagar *et al.* (1954) have expressed the collision operator as a relaxation towards an equilibrium state (which for kinetic theory of gases corresponds to the lattice-discretized Maxwell distribution) and through which the flow dynamics can satisfy the Navier-Stokes equations, under the condition that some unphysical high order terms that appear due to the discretization remain low. More recently developed lattice-Boltzmann methods operate the relaxation in a projection of the probabilities (f) on another basis than lattice velocities ($\vec{c}_i$), which allows to relax different combinations of their moments with different relaxation coefficients. Such Multiple-Relaxation-Time (MRT) approaches (D'Humières *et al.*, 2002) offer a way to segregate between physical and unphysical terms in the equation and to damp the unphysical high order terms, widening the set of conditions under which Navier-Stokes equations are satisfied with a good accuracy.

There is then a matrix $[P]$ to operate the projection between the probabilities and the set of moments that are relaxed. In this study, the collision operator described by Eggels and Somers (1995) is used. The relaxed moments are chosen so that flow field quantities directly appear in a so-called solu-

tion vector (q).

$$f(\vec{x}+\vec{c},t+1) = [\mathrm{P}]^{-1} \underbrace{([1]+[\Omega])\overbrace{[\mathrm{P}]\,f(\vec{x},t)}^{q^-}}_{q^+} \qquad (18)$$

$$q^{\pm} = \left| \begin{array}{l} \rho \\[4pt] \rho\vec{u} \pm \dfrac{1}{2}\vec{f} \\[8pt] \rho([\vec{u}\otimes\vec{u}]) + \rho\dfrac{\pm 1 - 6\nu}{6\nu}([\nabla\vec{u}]+[\nabla\vec{u}]^{\top}) \end{array} \right.$$

One of the nice properties of such a collision operator is that the external forces are applied during the collision step, and the projection matrix ($[\mathrm{P}]$) gives a direct relation between the probabilities (f) and the corresponding momentum change at each time step (that is the relaxation of the first order moments of the probabilities). It has been leveraged for the solid-liquid coupling method, as well as for boundary conditions, where shear stress was imposed as an external force to get a shear flow.

Immersed boundary method

Due to the ease to exchange momentum with the liquid phase through the chosen collision operator, the coupling with the solids is achieved using the momentum exchange based boundary developed by Niu *et al.* (2006). The surface of the particles is described by marker points, distributed as regularly as can be on the particle surface, each weighted to the area of the surface element it corresponds to, as shown on figure 2.

The coupling between the marker points (M) of the solids and the lattice nodes for the liquid is achieved by interpolating the quantities using regularized Dirac functions (δ) as described by Roma *et al.* (1999). The values of the probabilities are thus interpolated at the marker point position ($\vec{x}_M$), and the force contribution of each marker point to the coupling between the two phases is calculated using bounce-back (stopping the flow) and adding the momentum that corresponds to the solid phase at this position, weighted by surface element area. The resulting force ($\vec{f}_{p/f}$) is then distributed on the fluid
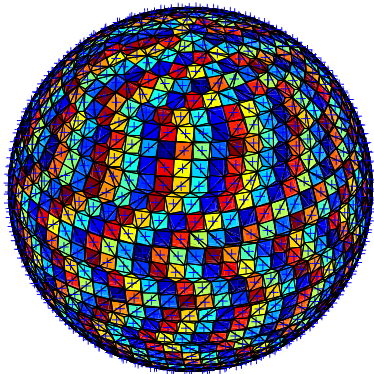
Figure 2: Representation of a sphere using a surface distribution of marker points ($+$) and their corresponding surface elements (each represented with a different color)
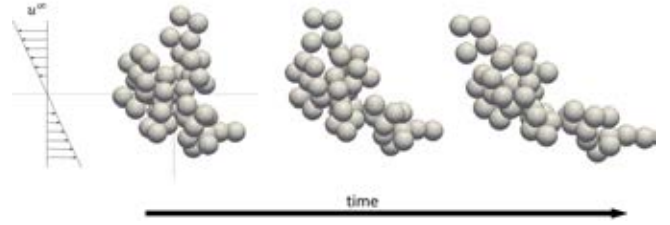
Figure 3: Aggregate 1 (see figure 1) placed in a pure shear flow so that its center of mass lies in the zero velocity plane

nodes using the same regularized Dirac function.

$$f_M = \sum_{\vec{x}} f(\vec{x})\,\delta(\vec{x}_M - \vec{x}) \qquad (19)$$

$$\vec{f}_M = \overbrace{\mathcal{A}_M}^{\text{marker weight}} \sum_i \left(\overbrace{f_M(-\vec{c}_i) - f_M(\vec{c}_i)}^{\text{full way bounce back}} + \overbrace{[\mathrm{P}]^{-1}_{(\vec{c}_i)}\rho\vec{u}_M}^{\text{solid velocity}} \right) \vec{c}_i \qquad (20)$$

$$\vec{f}_{p/f}(\vec{x}) = \sum_M \vec{f}_M\,\delta(\vec{x}_M - \vec{x}) \qquad (21)$$

Due to the way of computing the coupling force ($\vec{f}_{p/f}$), it ensures that the fluid velocity, after the collision operator is applied, is the velocity of the solid. On the other hand, the force and the torque acting on the solids are the sum of the reciprocal actions.

$$\vec{F}_{f/p} = -\sum_M \vec{f}_M \qquad (22)$$

$$\vec{T}^O_{f/p} = -\sum_M (\vec{x}_M - \vec{x}_O) \times \vec{f}_M \qquad (23)$$

Since this coupling method forces the fluid surface corresponding to the solid boundary to behave like a solid, the action of the fluid inside the solid must be cancelled. To do that, in the equation of motion that is solved in the DEM, another external force is applied to every resolved particle that opposes inner fluid inertia. To make sure that this force can be easily estimated, another surface boundary is forced inside the particle, so that viscous effects between the forced layers make the motion of the inner fluid follow a solid body motion.

Then, the inertia of the inner fluid should be removed by introducing a virtual force in the DEM as a coefficient for the acceleration term, see α in equation (5), but here, since the particle density and the fluid density are the same it would have made the equation degenerate. Inner fluid inertia has been kept for numerical reasons, but it has no impact on the physical results since particle Stokes number is very low anyway.

Simulation cases

Initial aggregates as presented in figure 1 were introduced in laminar pure shear flows, as shown is figure 3. Aggregates restructure due to the forces it experiences from the flow and the fractal dimensions (D_f) are recorded over time.

To study the relative effect of the different forces on the evolution of fractal dimension, several variations of the forces were considered. Equations 9 and 10 show that for a given particle diameter, the maximum cohesive force depends on the Hamaker constant A_H. For clay colloidal systems, A_H is generally of the order 10^{-20} J and Born (N_{Born}) constant can have values between 10^{-18} to 10^{-23}, which gives maximum cohesive force in the order 10^{-9} N. Pantina and Furst (2005)

A_H **(J)**	$(F_n)_\text{max}$ **(N)**	k_t **(N/m)**	$(F_t)_\text{max}$ **(N)**	$\dot{\gamma}$ **(s^{-1})**	$(F_{f/p})_\text{max}$ **(N)**
5.92×10^{-21}	10^{-9}	2.5×10^{-2}	10^{-9}	2652.59	10^{-9}
5.92×10^{-22}	10^{-10}	2.5×10^{-3}	10^{-10}	265.259	10^{-10}
5.92×10^{-23}	10^{-11}	2.5×10^{-4}	10^{-11}	26.5259	10^{-11}

Table 1: Simulation parameters: values of the physical constants and corresponding maximum forces

suggest that the maximum tangential force is of the order 10^{-11} N. Also, it is common to see shear rates of $100\,\text{s}^{-1}$ in experiments involving colloidal aggregates. The maximum shear-induced force between two particles can be estimated based on the drag force and the variation of velocity across a particle diameter.

$$F_{f/p} \sim 12\pi\mu\dot{\gamma}R_p^2 \qquad (24)$$

The cohesive interactions within the whole aggregate will need to balance the driving force. However, these cohesive interactions are summed over chains of particles that all see different flow velocities. In the 50 particle aggregates, particle chains are about a dozen of primary particles long. This is why the estimation of $(F_{f/p})_\text{max}$ was increased by an order of magnitude than the calculated value from equation (24). For a clay colloidal system with primary particles that would be $2\,\mu m$ in diameter, this gives a value of the order of 10^{-10} N.

The reference case was then chosen with a maximum attraction force $((F_n)_\text{max} = \max(\|\vec{F}_\text{VDW} + \vec{F}_\text{Born}\|))$ of 10^{-9} N, a maximum tangential force $((F_{tang.})_\text{max})$ of 10^{-11} N and a shear induced force $((F_{f/p})_\text{max})$ of 10^{-10} N. To reflect the relative variations of these parameters, forces have been expressed as their ratio to the shear induced force, which were then varied from 0.01 to 100. Table 1 lists all the physical values A_H, k_t and $\dot{\gamma}$ that have been varied for the simulations, and their corresponding force magnitudes. Table 2 lists all the simulation cases and the corresponding force ratios. In such conditions, the Reynolds number, calculated based on the shear rate, varies from 10^{-4} to 10^{-2}.

The LBM and DEM schemes used for this research follow the same approach as described in Kroll-Rabotin *et al.* (2012). In this study, the simulations were performed in a domain of 200^3 nodes, with each node of size $0.2\mu m$. Time step for each iteration was of the order 10^{-9} s.

RESULTS AND DISCUSSION

Fractal Dimension as a morphology indicator

To address the question of the relevance of fractal dimensions (D_f) as the single morphology indicator, all tested conditions have been repeated for 10 aggregates with the same fractal dimension. The number of particles and the primary particle diameter were always kept constant.

Figure 4 shows the evolution over time of the fractal dimension of the 10 aggregates (see figure 1) for various force ratios. Although it is hard to make any quantiative observation from such different curves, all these plots show that in all cases, all 10 aggregates follow the same trend and undergo the overall same transformation after some time, be it breakage or reaching about the same fractal dimension. The behaviour of aggregates number 8 (in the second line) and number 7 (right hand side of the third line) give confidence in the fact that observations extracted from the whole set of aggregates can be interpreted as general rules. Indeed, its apparent initial imbalance makes it behave quite differently from all other aggregates during most simulation's early stages.

However, after some morphological evolution, it ends up following the same trends and reach the same fractal dimension as all the others. The final states that are observed thus seem not to be too dependent on the initial structure of the aggregates.

Due to the negligible inertia in different cases, the evolution trends of the aggregate morphologies did not depend on the force magnitudes, only the time scale of the problem would change. As a consequence, cases with the same force ratios were not repeated to see effectiveness of D_f as the single morphological parameter. Table 2 lists all the cases that have been considered along with the resulting morphological evolution of the aggregates. When aggregates did not break, their morphology has been characterized by their time averaged fractal dimension over a rotation. Indeed, the antisymmetric part of the deformation rate in the flow corresponds to a rotation with a revolution period of $4\pi/\dot{\gamma}$. Since aggregates never stop rotating in such a flow, and their fractal dimension may keep changing with their orientation relative to the shear direction, only time averaged fractal dimensions ($\langle D_f \rangle$) displayed in table 2.

$$\langle D_f \rangle = \lim_{\tau \to \infty} \frac{1}{4\pi/\dot{\gamma}} \int_{\tau - 4\pi/\dot{\gamma}}^{\tau} D_f \, dt \qquad (25)$$

Several force ratios yield aggregate breakage, in which case it is meaningless to compare the fractal dimension of the parts to the one of the initial aggregate, since the limited number of particles in aggregates has a strong influence on the fractal dimension. In such cases, the time before breakage of the aggregate in such conditions is reported in table 2, since this is the most significant parameter to capture the breakage rate in population balance studies that could make use of the results presented here.

Relative effect of the different force components

In table 2, highlighted cells in light red are those which broke during the simulation run, while those in grey broke in the very beginning of the simulation.

When shear prevails compared to attractive forces ($(F_n^*) < 1$), aggregates break immediately. This can obviously be explained since normal forces are the ones that oppose the tearing apart of primary particles, and prevent the aggregate from breaking. Aggregate cohesion in the end boils down to cohesive interactions between primary particles. However, as soon as there is enough cohesion between primary particles, the way forces are distributed within the aggregate will vary depending on the relative contributions of the tangential and normal interactions.

When (F_n^*) is kept constant, tangential forces appear to have a significant impact on aggregate breakage or structure. Increasing (F_t^*) tends to favor aggregate breakage. Indeed, as general rule of thumb tangential forces within the aggregate reduce the normal forces between particles. If forces acting on an aggregate are transmitted between primary particle through tangential interactions, there is less attractive contribution opposing the total tearing force, which means that
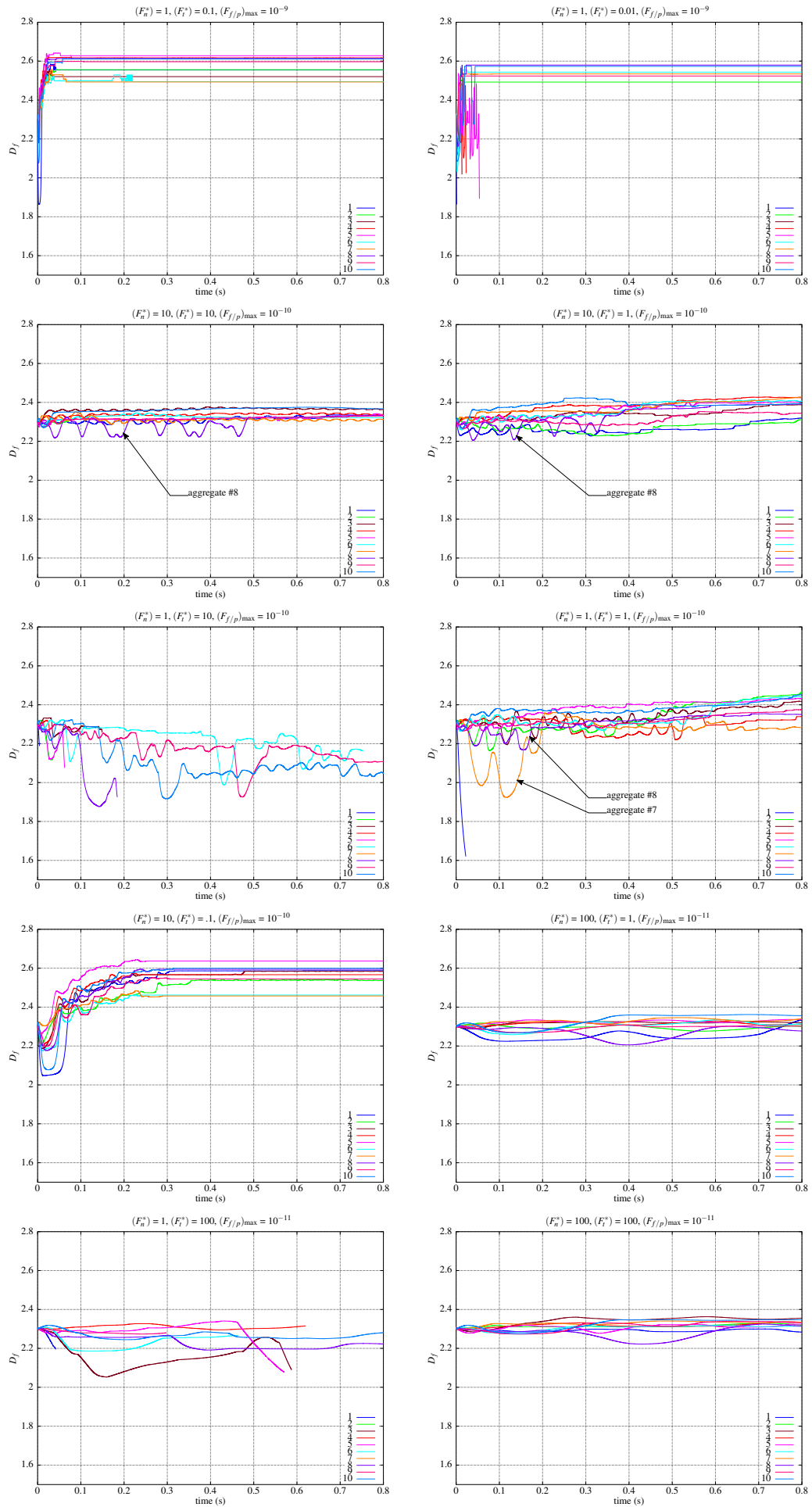
Figure 4: Evolution of fractal dimension (D_f) over time for several force ratios. Lines stopping before the end of the time axis mean that the corresponding aggregate broke in such conditions.

$(F_{f/p})_{max}$	(F_n^*)	(F_t^*)	Aggregate label (see figure 1)									
			1	2	3	4	5	6	7	8	9	10
10^{-11}	1	1	44.0	2.2579	2.3057	2.3183	2.2806	2.3188	2.0364	2.2106	2.2954	2.3524
10^{-11}	1	10	44.0	248.0	2.3218	752.0	644.0	2.2626	67.0	2.2085	2.2878	2.2971
10^{-11}	1	100	42.0	14.0	587.56	620.0	570.6	464.0	16.0	2.2043	298.0	2.2628
10^{-11}	10	1	2.2483	2.2793	2.3218	2.3171	2.3120	2.3093	2.3398	2.2592	2.2982	2.3608
10^{-11}	10	10	2.2979	2.2961	2.3574	2.3271	2.3113	2.3098	2.3136	2.2759	2.3043	2.3485
10^{-11}	10	100	2.2995	2.2818	2.2944	2.3074	2.2991	2.3168	68.04	2.2769	2.3055	2.3481
10^{-11}	100	1	2.2611	2.2924	2.3219	2.3155	2.3275	2.3173	2.3331	2.2607	2.3021	2.3575
10^{-11}	100	10	2.3155	2.295	2.3131	2.3269	2.3351	2.3135	2.3219	2.2754	2.3073	2.3437
10^{-11}	100	100	2.2928	2.3181	2.3531	2.3195	2.3114	2.3137	2.3342	2.2736	2.3295	2.3454
10^{-10}	0.1	0.1	0.2	0.12	0.2	1.12	0.16	0.24	0.2	0.2	0.2	0.16
10^{-10}	0.1	1	0.12	0.08	0.08	0.08	0.08	0.08	0.08	0.04	0.08	0.04
10^{-10}	0.1	10	0.08	0.12	0.04	0.2	0.04	0.16	0.04	0.04	0.08	0.04
10^{-10}	1	0.1	2.6101	2.5396	2.6218	2.6094	2.6200	2.5492	2.4305	2.6330	2.6223	2.5729
10^{-10}	1	1	5.2	2.4513	2.4131	2.327	2.4308	2.3605	2.2812	2.3508	2.371	2.4401
10^{-10}	1	10	4.32	38.16	149.2	28.8	62.52	753.2	6.68	184.2	2.1066	2.0403
10^{-10}	10	0.1	2.5875	2.5370	2.5839	2.5666	2.6371	2.4621	2.4574	2.5947	2.5449	2.5992
10^{-10}	10	1	2.3161	2.2998	2.3875	2.4255	2.4025	2.4078	2.4232	2.3905	2.3423	2.3926
10^{-10}	10	10	2.3342	72	2.3646	2.3379	2.3346	2.3220	2.3103	2.3325	2.3304	2.3676
10^{-09}	0.01	0.01	0.04	0.04	0.04	0.04	0.04	0.04	0.04	0.04	0.04	0.04
10^{-09}	0.01	0.1	0.04	0.04	0.04	0.04	0.04	0.04	0.04	0.04	0.04	0.04
10^{-09}	0.01	1	0.04	0.08	0.04	0.04	0.04	0.04	0.04	0.04	0.04	0.04
10^{-09}	0.1	0.01	0.24	0.28	0.56	0.2	0.24	0.16	0.04	0.48	0.04	0.16
10^{-09}	0.1	0.1	0.16	0.16	0.04	0.12	0.04	0.32	0.04	0.04	0.04	0.04
10^{-09}	0.1	1	0.24	0.04	0.04	0.04	0.04	0.04	0.04	0.04	0.04	0.04
10^{-09}	1	0.01	1.12	2.4923	13.48	23.08	53.8	2.5436	2.5342	2.5799	2.5237	2.5734
10^{-09}	1	0.1	2.5546	2.5559	2.5205	2.6169	2.6278	2.4944	2.4929	2.6138	2.5969	2.6111
10^{-09}	1	1	0.56	2.6076	2.5966	2.5247	2.6154	2.5426	2.5405	2.5636	2.5354	2.5772

Table 2: Overview of the simulation results in terms of fractal dimension ($\langle D_f \rangle$) or time undergoing shear (in milliseconds) until breakage (in highlighted cells) for all 10 aggregates. Cells in grey indicate that the aggregates broke at the very beginning of the simulation. In cases highlighted in red, aggregates broke after significant morphological evolution.

$(F_{f/p})_{max}$	(F_n^*)	(F_t^*)	Aggregate label (see figure 1)									
			1	2	3	4	5	6	7	8	9	10
10^{-11}	1	1	2.1897									
10^{-11}	1	10	2.1839	2.1254		2.2886	2.0721		2.3174			
10^{-11}	1	100	2.1949	2.3079	2.0888	2.3153	2.077	2.2667	2.3019		2.28	
10^{-11}	10	100							2.3183			
10^{-10}	0.1	0.1	2.2966	2.3016	2.298	2.2979	2.302	2.3049	2.3	2.3053	2.2967	2.2999
10^{-10}	0.1	1	2.2979	2.3012	2.2989	2.303	2.3014	2.3047	2.2998	2.3049	2.2963	2.2995
10^{-10}	0.1	10	2.2986	2.2998	2.2992	2.2991	2.3019	2.3042	2.2993	2.3043	2.2958	2.2991
10^{-10}	1	1	2.1487									
10^{-10}	1	10	2.188	2.138	2.2568	2.2377	2.0754	2.1651	2.3176	1.9251		
10^{-10}	10	10		2.3007								
10^{-09}	0.01	0.01	2.2887	2.2961	2.2921	2.2974	2.3002	2.3052	2.3027	2.3001	2.2988	2.3061
10^{-09}	0.01	0.1	2.2872	2.2937	2.2895	2.2953	2.2953	2.3022	2.2998	2.2952	2.2949	2.3017
10^{-09}	0.01	1	2.2851	2.2744	2.2873	2.2938	2.2904	2.2979	2.2969	2.2924	2.289	2.2982
10^{-09}	0.1	0.01	2.1961	2.2205	2.0394	2.2584	2.2624	2.2927	2.3048	2.3031	2.3017	2.3091
10^{-09}	0.1	0.1	2.238	2.2515	2.2938	2.2781	2.2975	2.2133	2.302	2.2979	2.298	2.3054
10^{-09}	0.1	1	2.1839	2.2911	2.2898	2.2958	2.2925	2.3014	2.2989	2.2924	2.2924	2.3007
10^{-09}	1	0.01	1.8635		2.0177	2.0238	1.8928					
10^{-09}	1	1	2.1292									

Table 3: Instantaneous fractal dimension (D_f) just before breakage (see table 2)
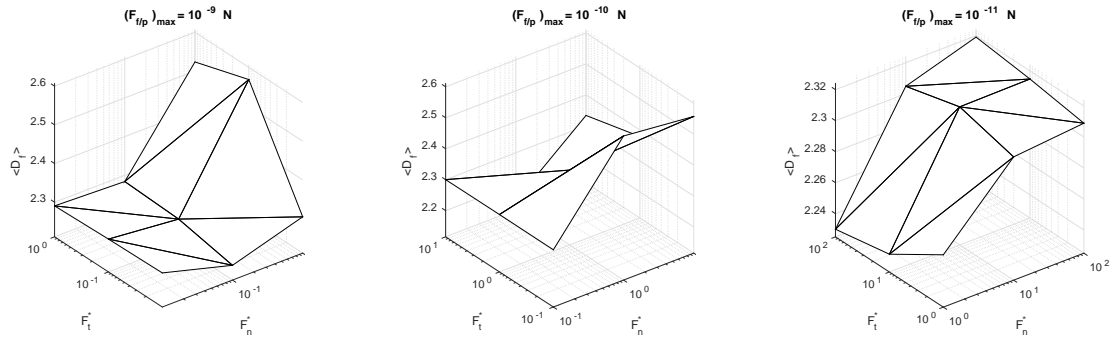
Figure 5: Mean fractal dimension as a function of the two interaction force contributions
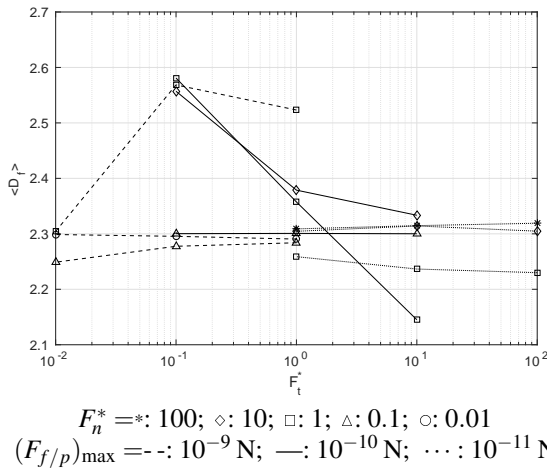

$F_n^* =$ *: 100; ⋄: 10; □: 1; △: 0.1; ○: 0.01
$(F_{f/p})_{\max} =$ - -: 10^{-9} N; —: 10^{-10} N; $\cdots$: 10^{-11} N

Figure 6: Evolution of the mean fractal dimension as a function of tangential interactions

$F_n^* =$ *: 100; ⋄: 10; □: 1; △: 0.1; ○: 0.01
$(F_{f/p})_{\max} =$ - -: 10^{-9} N; —: 10^{-10} N; $\cdots$: 10^{-11} N
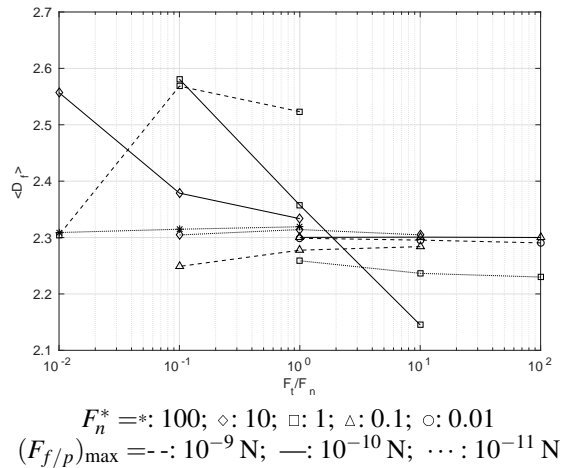
Figure 7: Evolution of the mean fractal dimension as a function of the ratio of the two components of particle interactions

the tearing force must oppose a weaker net attractive force in order to break the aggregate.

Comparing the final fractal dimension ($\langle D_f \rangle$) of aggregates in conditions where they do not break, shows the impact of the different force contributions on the final shape of the aggregate. As expected, when (F_n^*) varies while (F_t^*) remains constant, aggregates tend to be denser: they show a higher fractal dimension. Conversely, the higher ($F_{f/p}$)$_{\max}$ (in the non-breaking range), the higher $\langle D_f \rangle$.

However, the dependence of fractal dimension on the tangential force ratio (F_t^*), when other forces are kept constant, shows that the rule of thumb derived from breakage observation only captures very approximately the role of such forces. Indeed, figure 5 shows that their actual impact differs depending on other parameters, such as the value of (F_n^*), but there is no clear trend. Some cases show a steep decrease of the fractal dimension when F_t^* increases, but others, corresponding to relatively high values of F_n^*, show an inverse relation, though in a much less sensitive manner.

Another way to look at the relative effects of the different forces is presented in figure 6. In this figure, a single value for the fractal dimension is reported for every simulated condition, it is calculated by averaging all the fractal dimensions of the 10 aggregates, with the aim to observe general trends. In order to try to capture as much morphological evolutions as possible in this single characteristic value, in cases where aggregates broke, their instantaneous fractal dimension at the instant they broke was used for the averaging step. These instantaneous fractal dimensions D_f are shown in table 3.

All curves in figures 6 and 7 relate evolutions of the fractal dimension to the tangential force ratio, for various combinations of the other forces. Tangential force ratios have been scaled relatively to the drag (figure 6) and to the normal force component figure 7) but none of these comparisons show any definite trend. There is an expected overall tendency of the fractal dimension to increase when tangential interactions are low, however, the most striking feature of figures 6 and 7 is the particularly high number of data points that fall outside of the main trend.

Results from IBM

Since free draining approximation does not account for the flow perturbation induced by particles on the force acting on every particles, results from such an assumption are expected to be inaccurate in cases where fractal dimension (D_f) increases to high values over time. A few simulations were run with fully resolved flows using an LBM+IBM approach, to account for the impact of multiphase coupling on the aggregate behaviour.

Figure 8 shows how aggregate number 1 evolved under high shear and with interaction forces of the same order of magnitude as the shear induced force. First, in such conditions, this aggregate broke quickly when using the free draining approximation, while the LBM+IBM simulation did not give such result. This difference, in itself, shows an obvious impact of the coupling on the aggregate behaviour. Now, when looking at the flow perturbation induced by the presence of the aggregate in the pure shear, this tells a little more about
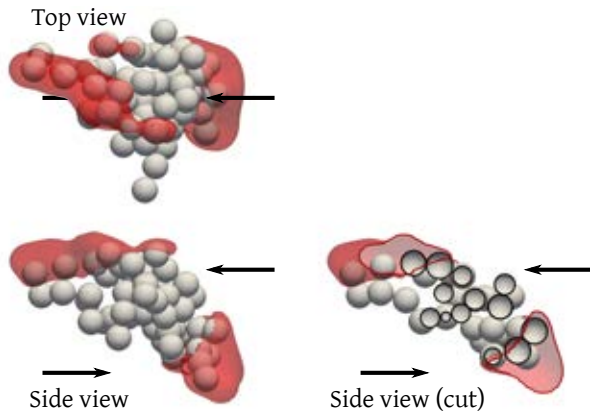
Top view

Side view   Side view (cut)

Figure 8: Aggregate 1 (see figure 1) after 1.2 ms under similar conditions as the last line of table 2 but resolved with LBM+IBM. The red surface is an iso-surface of the velocity perturbation for the characteristic velocity difference due to the shear at the scale of primary particles, see (26)

the difference in behaviour.

The flow perturbation is represented with an iso-surface of the velocity difference between the pure shear and the resolved flow with the aggregate. The value corresponding of the iso-surface is the velocity scale given by the shear rate and the diameter of primary particles.

$$\|\vec{v} - \dot{\gamma} z \vec{e}_x\| = 2\dot{\gamma} R_p \qquad (26)$$

The arrows on figure 8 show the liquid velocity direction, and consequently the shear experienced by the aggregate. From this, it clearly appears that particle chains aligned with the flow are shielded by the aggregate region that faces the flow. Many particles, inside the red bubbles, are much more protected from the shear forces than what is considered in the free draining approximation.

Simulations with resolved flows take much longer to run, but also, the complex nature of the hydrodynamic interactions between particles make them hard to study in a similar way as what has been done with fractal dimension. To capture their impact and shed light on some trends, many more simulations must be run, but more importantly pre- and post processing tools and methods must be developed so that the simulation results can be properly interpreted.

CONCLUSION

In this work, a preliminary attempt at understanding the relative roles of the multiple forces acting within an aggregate undergoing shear has been presented. While the effect of cohesive forces and shear forces was well established, the relative study of tangential forces showed that their combined effect with other forces is complex. Although no quantitative observations nor clear tendencies depending with respect to other forces could be derived from the results, it was confirmed that tangential forces tend to decrease the cohesive forces within the aggregate. Although the force ratios that characterize the flow conditions and aggregate properties in this study seem similar to Shields numbers, as commonly defined to characterize granular flows (Ouriemi *et al.*, 2009) the systems that it was applied to are too different from ours to directly correlate our study with them. The elastic nature of the interactions within colloidal systems, and the importance of discrete interactions in relatively small aggregates yield

very different behaviours so that no critical Shields number seem to characterize aggregate restructuring.

This work is a pioneer in using IBM to couple solids with fluid in aggregate restructuring studies. The behaviour of an aggregate as simulated using LBM+IBM was compared to its free draining approximation counterpart. It showed that there is a significant difference in aggregate behavior when hydrodynamic interactions are taken into account. Thus, numerical simulations with LBM+IBM will give more accurate results than free draining approximation, as the flow perturbations due to every particles will be fully resolved.

Finally, all these preliminary numerical investigations already confirmed a few expected restructuring behaviours, and illustrated the complexity of studying aggregate restructuring even under very controlled conditions, with simplified interactions. But more importantly, they have demonstrated the feasibility and the suitability of the LBM+DEM+IBM approach for such a problem, and confirmed the need for such numerical investigations. Now that the method has been developed and applied to this problem, more extensive studies covering various interactions and flow conditions involving higher Reynolds and Stokes numbers promise to yield valuable knowledge on aggregate restructuring.

REFERENCES

ADLER, P.M. and MILLS, P.M. (1979). "Motion and rupture of a porous sphere in a linear flow field". *Journal of Rheology*, **23(1)**, 25–37.

BAGSTER, D.F. and TOMI, D. (1974). "The stresses within a sphere in simple flow fields". *Chemical Engineering Science*, **29(8)**, 1773–1783.

BECKER, V. and BRIESEN, H. (2008). "Tangential-force model for interactions between bonded colloidal particles". *Physical Review E*, **78(6)**, 061404.

BECKER, V., SCHLAUCH, E., BEHR, M. and BRIESEN, H. (2009). "Restructuring of colloidal aggregates in shear flows and limitations of the free-draining approximation". *Journal of Colloid and Interface Science*, **339(2)**, 362–372.

BHATNAGAR, P.L., GROSS, E.P. and KROOK, M. (1954). "A model for collision processes in gases. I. small amplitude processes in charged and neutral one-component systems". *Physical Review*, **94**, 511–525.

BINDER, C., FEICHTINGER, C., SCHMID, H.J., THÜREY, N., PEUKERT, W. and RÜDE, U. (2006). "Simulation of the hydrodynamic drag of aggregated particles". *Journal of Colloid and Interface Science*, **301(1)**, 155–167.

BRADY, J.F. and BOSSIS, G. (1988). "Stokesian dynamics". *Annual Review of Fluid Mechanics*, **20(1)**, 111–157.

BUSHELL, G.C., YAN, Y.D., WOODFIELD, D., RAPER, J. and AMAL, R. (2002). "On techniques for the measurement of the mass fractal dimension of aggregates". *Advances in Colloid and Interface Science*, **95(1)**, 1–50.

CHEN, D. and DOI, M. (1989). "Simulation of aggregating colloids in shear flow. II". *The Journal of Chemical Physics*, **91(4)**, 2656–2663.

CONCHUIR, B.O., HARSHE, Y.M., LATTUADA, M. and ZACCONE, A. (2014). "Analytical model of fractal aggregate stability and restructuring in shear flows". *Industrial & Engineering Chemistry Research*, **53(22)**, 9109–9119.

COUFORT, C., BOUYER, D. and LINÉ, A. (2005). "Flocculation related to local hydrodynamics in a Taylor-Couette reactor and in a jar". *Chemical Engineering Science*, **60(8)**, 2179–2192.

CUNDALL, P.A. and STRACK, O.D. (1979). "A discrete

numerical model for granular assemblies". *Geotechnique*, **29(1)**, 47–65.

DAOUD, I.L.A., RIMBERT, N., JARDY, A., OESTERLÉ, B., HANS, S. and BELLOT, J.P. (2011). "3d modeling of the aggregation of oxide inclusions in a liquid steel ladle: two numerical approaches". *Advanced Engineering Materials*, **13**, 543–549.

D'HUMIÈRES, D., GINZBURG, I., KRAFCZYK, M., LALLEMAND, P. and LUO, L.S. (2002). "Multiple-relaxation-time lattice Boltzmann models in three dimensions". *Philosophical Transactions of the Royal Society of London A: Mathematical, Physical and Engineering Sciences*, **360**, 437–451.

DOMINIK, C. and NÜBOLD, H. (2002). "Magnetic aggregation: dynamics and numerical modeling". *Icarus*, **157(1)**, 173–186.

EGGELS, J.G.M. and SOMERS, J.A. (1995). "Numerical simulation of free convective flow using the lattice-Boltzmann scheme". *International Journal of Heat and Fluid Flow*, **16(5)**, 357–364.

EGGERSDORFER, M.L., KADAU, D., HERRMANN, H.J. and PRATSINIS, S.E. (2010). "Fragmentation and restructuring of soft-agglomerates under shear". *Journal of Colloid and Interface Science*, **342(2)**, 261–268.

FEKE, D.L., PRABHU, N.D., MANN, J.A.J. and MANN, J.A.L. (1984). "A formulation of the short-range repulsion between spherical colloidal particles". *The Journal of Physical Chemistry*, **88(23)**, 5735–5739.

FRUNGIERI, G. and VANNI, M. (2016). "Dynamics of a shear-induced aggregation process by a combined Monte Carlo-Stokesian dynamics approach". *International Conference on Multiphase Flow*. Firenze.

GMACHOWSKI, L. (2002). "Calculation of the fractal dimension of aggregates". *Colloids and Surfaces A: Physicochemical and Engineering Aspects*, **211(2)**, 197–203.

GREGORY, J. (1997). "The density of particle aggregates". *Water Science and Technology*, **36(4)**, 1–13.

HAMAKER, H.C. (1937). "The London-van der Waals attraction between spherical particles". *Physica*, **4(10)**, 1058–1072.

HARSHE, Y.M. and LATTUADA, M. (2012). "Breakage rate of colloidal aggregates in shear flow through Stokesian dynamics". *Langmuir*, **28(1)**, 283–292.

HARSHE, Y.M., LATTUADA, M. and SOOS, M. (2011). "Experimental and modeling study of breakage and restructuring of open and dense colloidal aggregates". *Langmuir*, **27(10)**, 5739–5752.

IWASHITA, K. and ODA, M. (1998). "Rolling resistance at contacts in simulation of shear band development by DEM". *Journal of Engineering Mechanics*, **124(3)**, 285–292.

KADAU, D., BARTELS, G., BRENDEL, L. and WOLF, D.E. (2002). "Contact dynamics simulations of compacting cohesive granular systems". *Computer Physics Communications*, **147(1-2)**, 190–193.

Khashayar Rastegari, William Y. Svrcek and YARRANTON*, H.W. (2004). "Kinetics of asphaltene flocculation". *Industrial & Engineering Chemistry Research*, **43(21)**, 6861–6870.

KROLL-RABOTIN, J.S., SUNGKORN, R., HASHEMI, S.A., DERKSEN, J.J. and SANDERS, R.S. (2012). "Large eddy simulation of a solid-liquid fluidized bed using the lattice-boltzmann method and a soft-sphere collision model". *Proc. Ninth Int. Conference on CFD in Minerals and Process Industries*. Melbourne, Australia.

LĀCIS, U., TAIRA, K. and BAGHERI, S. (2016). "A stable fluid-structure interaction solver for low-density rigid bodies using the immersed boundary projection method". *Journal of Computational Physics*, **305**, 300–318.

LASKOWSKI, J.J. and RALSTON, J. (2015). *Colloid chemistry in mineral processing*. Elsevier.

LI, D.H. and GANCZARCZYK, J. (1989). "Fractal geometry of particle aggregates generated in water and wastewater treatment processes". *Environmental science & technology*, **23(11)**, 1385–1389.

NIU, X.D., SHU, C., CHEW, Y.T. and PENG, Y. (2006). "A momentum exchange-based immersed boundary-lattice Boltzmann method for simulating incompressible viscous flows". *Physics Letters A*, **354**, 173–182.

OURIEMI, M., AUSSILLOUS, P. and GUAZZELLI, E. (2009). "Sediment dynamics. part 1. bed-load transport by laminar shearing flows". *Journal of Fluid Mechanics*, **636**, 295–319.

PANTINA, J.P. and FURST, E.M. (2005). "Elasticity and critical bending moment of model colloidal aggregates". *Physical Review Letters*, **94(13)**, 138301.

PESKIN, C.S. (1972). "Flow patterns around heart valves: a numerical method". *Journal of Computational Physics*, **10(2)**, 252–271.

PLUMPTON, A.J. (2013). *Production and Processing of Fine Particles: Proceedings of the International Symposium on the Production and Processing of Fine Particles, Montreal, August 28-31, 1988*. Elsevier.

POTANIN, A.A. (1993). "On the computer simulation of the deformation and breakup of colloidal aggregates in shear flow". *Journal of Colloid and Interface Science*, **157(2)**, 399–410.

REN, Z., HARSHE, Y.M. and LATTUADA, M. (2015). "Influence of the potential well on the breakage rate of colloidal aggregates in simple shear and uniaxial extensional flows". *Langmuir*, **31(21)**, 5712–5721.

ROMA, A.M., PESKIN, C.S. and BERGER, M.J. (1999). "An adaptive version of the immersed boundary method". *Journal of Computational Physics*, **153**, 509–534.

SCHLAUCH, E., ERNST, M., SETO, R., BRIESEN, H., SOMMERFELD, M. and BEHR, M. (2013). "Comparison of three simulation methods for colloidal aggregates in Stokes flow: finite elements, lattice Boltzmann and Stokesian dynamics". *Computers & Fluids*, **86**, 199–209.

SETO, R., BOTET, R., AUERNHAMMER, G.K. and BRIESEN, H. (2012). "Restructuring of colloidal aggregates in shear flow". *The European Physical Journal E*, **35(12)**, 128.

SMOLUCHOWSKI, M.V. (1917). "Grundriß der Koagulationskinetik kolloider Lösungen". *Kolloid-Zeitschrift*, **21(3)**, 98–104.

SONNTAG, R.C. and RUSSEL, W.B. (1987). "Structure and breakup of flocs subjected to fluid stresses". *Journal of Colloid and Interface Science*, **115(2)**, 390–395.

TAIRA, K. and COLONIUS, T. (2007). "The immersed boundary method: a projection approach". *Journal of Computational Physics*, **225(2)**, 2118–2137.

VAEZI G., F., SANDERS, R.S. and MASLIYAH, J.H. (2011). "Flocculation kinetics and aggregate structure of kaolinite mixtures in laminar tube flow". *Journal of Colloid and Interface Science*, **355**, 96–105.

VANNI, M. and GASTALDI, A. (2011). "Hydrodynamic forces and critical stresses in low-density aggregates under shear flow". *Langmuir*, **27(21)**, 12822–12833.

WOODFIELD, D. and BICKERT, G. (2001). "An im-

proved permeability model for fractal aggregates settling in creeping flow". *Water Research*, **35(16)**, 3801–3806.

YANG, J. and STERN, F. (2013). "Fully resolved simulation of particulate flow using a sharp interface direct forcing immersed boundary method". *ASME 2013 Fluids Engineering Division Summer Meeting*, V01AT08A006. ASME, Nevada.

ZHANG, L. and THOMAS, B.G. (2003). "State of the art in evaluation and control of steel cleanliness." *ISIJ International*, **43(3)**, 271–291.